AGU PUBLICATIONS

JGR

Journal of Geophysical Research: Oceans

RESEARCH ARTICLE

10.1002/2016JC012662

Intraseasonal-to-semiannual variability of sea-surface height in the astern, equatorial Indian Ocean and southern Bay of Bengal

Xuhua Cheng[1,2,3], Julian P. McCreary[2], Bo Qiu[4], Yiquan Qi[1], and Yan Du[1]

[1]State Key Laboratory of Tropical Oceanography, South China Sea Institute of Oceanology, Chinese Academy of Sciences, Guangzhou, China, [2]International Pacific Research Center, University of Hawaii at Manoa, Honolulu, Hawaii, USA, [3]College of Oceanography, Hohai University, Nanjing, China, [4]Department of Oceanography, University of Hawaii at Manoa, Honolulu, Hawaii, USA

Key Points:
- 30–60 day SSH variability is strong in the southern BoB and along the coast of Sumatra
- Eddies propagating from the east play a primary role in SSH variability east of Sri Lanka, indicating the importance of nonlinear processes
- In the southern BoB, the $n = 2$ mode is dominant at 180 days, due to basin resonance and strong wind forcing

Correspondence to:
X. Cheng,
xuhuacheng@scsio.ac.cn

Citation:
Cheng, X., J. P. McCreary, B. Qiu, Y. Qi, and Y. Du (2017), Intraseasonal-to-semiannual variability of sea-surface height in the astern, equatorial Indian Ocean and southern Bay of Bengal, *J. Geophys. Res. Oceans, 122*, doi:10.1002/2016JC012662.

Received 28 DEC 2016
Accepted 24 APR 2017
Accepted article online 27 APR 2017

Abstract Intraseasonal-to-semiannual variability of sea-surface height (SSH) in the eastern, equatorial Indian Ocean (EEIO) and southern Bay of Bengal (BoB) is investigated using altimetric data, and solutions to $1\frac{1}{2}$ layer (first baroclinic mode) and linear, continuously stratified (LCS; multibaroclinic-mode) models. The amplitude and dominant periods of SSH variability differ regionally. Large-amplitude variability is found along the west coast of Sumatra, in a zonal band across the BoB centered along 5°N, east of Sri Lanka, and in the northwestern BoB, respectively. Along the Sumatran west coast, SSH variability peaks at 30–60, 90, and 180 days. Along 5°N and east of Sri Lanka, the 30–60 day variability is dominant. Sensitivity experiments using a nonlinear version of the $1\frac{1}{2}$ layer model forced by realistic winds reproduce the observed patterns of intraseasonal variability in the southern BoB. At 30–60 days, the solutions show that eddies (nonlinear Rossby waves) propagating from the east, rather than local wind forcing, account for most of the variance east of Sri Lanka; furthermore, they demonstrate that the variance is significantly enhanced by the nonlinear transfer of 90–120 day energy into the intraseasonal band of 30–60 days. The LCS solutions show that the first two baroclinic modes explain most of the SSH variance at 90–180 days. The second baroclinic mode dominates the SSH variance at 180 days, a consequence of basin resonance and strong wind forcing.

1. Introduction

Recently, a number of studies have begun to explore intraseasonal (periods less than 90 days) variability in the Bay of Bengal (BoB) [e.g., *Vialard et al*., 2009; *Vinayachandran et al*., 2012; *Cheng et al*., 2013; *Girishkumar et al*., 2011, 2013; *Suresh et al*., 2013]. Using altimetry data and an eddy-resolving model, *Cheng et al*. [2013] reported large intraseasonal variability of sea-surface height (SSH) around the perimeter of the BoB, in a zonal band across the Bay centered near 5°N, and in the western BoB. Thermocline depths derived from temperature data from moored buoys in the BoB also show persistent intraseasonal variability at 30–120 days [*Girishkumar et al*., 2013]. A considerable part of this variability has been considered to be linked to equatorial forcing [*Vialard et al*., 2009; *Cheng et al*., 2013; *Girishkumar et al*., 2013; *Suresh et al*., 2013].

Intraseaonal-to-semiannual signals in the equatorial ocean have been extensively studied [e.g., *Han et al*., 2001; *Han* 2005; *Iskandar and McPhaden*, 2011; *Schott et al*., 2009; *Miyama et al*., 2006; *Webber et al*., 2010; *Han et al*., 2011; *Chen et al*., 2015]. It exhibits enhanced power at 40–60, 90, and 120 days. The 40–60 day band is forced by winds associated with the Madden-Julian Oscillation (MJO) [*Han et al*., 2001; *Oliver and Thompson*, 2010]. The longer-period signals are also forced by equatorial winds, but appear to be strengthened by basin resonances: *Han et al*. [2011] argue that resonances involving equatorial Kelvin and Rossby waves associated with the second (first) baroclinic mode enhance the 90 day (120 day) signal. Similarly, semiannual variability also appears to be strengthened by a basin resonance involving second-baroclinic-mode waves [*Jensen*, 1993; *Han et al*., 1999, 2011].

The equatorial variability propagates into the BoB as coastal Kelvin waves, and the eastern-coastal signal propagates westward via Rossby waves to impact the interior of the BoB [*Vialard et al*., 2009; *Cheng et al*., 2013; *Girishkumar et al*., 2013; *Suresh et al*., 2013]. Thermocline depths in the interior BoB are significantly influenced by the propagation of both first and second-baroclinic-mode Rossby waves from the eastern

boundary [*Girishkumar et al*., 2013]. Further, *Cheng et al*. [2013] and *Girishkumar et al*. [2013] noted that the Rossby waves cannot be linear: sometimes, they are interrupted, or appear more like propagating eddies, indicating that they are impacted by nonlinear processes.

We continue the effort to describe intraseasonal-to-semiannual SSH variability in the EEIO and BoB, and to understand the processes that cause it. For this purpose, we analyze satellite observations and existing OGCM output to identify the spatial and frequency structure of SSH variability in various subregions. In addition, to isolate the impacts of particular processes (wind forcing, nonlinearities, and higher-order baroclinic modes) in the southern BoB, we obtain solutions to two, simplified, ocean models, $1^1/_2$ layer (reduced-gravity) and linear, continuously stratified (LCS) models. The dynamics of variability in the northern BoB appears to be more complicated than in the southern Bay; in particular they seem to be baroclinically unstable, a process that our $1^1/_2$ layer and LCS models cannot simulate. For this reason, we delay a discussion of the dynamics in the northern BoB to a future study.

Key results are the following. In the southern BoB and especially east of Sri Lanka, intraseasonal SSH variance is dominated by 30–60 day signals. Rather than being forced by local winds, they are largely remotely forced by nonlinear Rossby waves (eddies), which are generated by the reflection of equatorial Kelvin waves from the eastern boundary. Solutions to nonlinear $1^1/_2$ layer model indicate the importance of nonlinear transfer of 90–120 day energy into the intraseasonal band. At 180 days, the second-baroclinic mode is dominant in the EEIO, due to basin resonance and strong wind forcing.

The paper is organized as follows. Section 2 describes the observational and OGCM data sets as well as the two simple dynamical models used for our analyses. Section 3 reports the prominent features of intraseasonal-to-semiannual SSH variability in the BoB using satellite observations and OGCM output. Section 4 explores the dynamics of 30–60 day variability in the southern BoB using the $1^1/_2$ layer model. Section 5 studies the generation mechanism of 90–180 day SSH variability using the LCS model. Finally, section 6 presents a summary of our results.

2. Data and Method

2.1. Sea-Level Data

In this study, the sea-level anomaly (SLA) data are obtained from Archiving, Validation, and Interpretation of Satellite Oceanographic data (AVISO, http://www.aviso.oceanobs.com/). The SLA data are a merged product from multiple satellite missions (T/P and ERS−1/2, followed by Jason−1, Jason−2, and Envisat). To remove the aliasing of tides and barotropic variability, a tidal model GOT2000 and a barotropic hydrodynamic model MOG2D−G are used to update the altimeter data [*Volkov et al*., 2007; *Dibarboure et al*., 2008]. The product is available on a $^1/_3°$ Mercator grid at a weekly interval and spans the period 1993–2012. The sea surface height (SSH) is the sum of SLA and mean dynamic topography, which is derived from GRACE data, altimetry measurements, and in situ observations [*Rio et al*., 2011].

We also use SSH data from an eddy-resolving OGCM for the Earth Simulator (OFES) [*Masumoto et al*., 2004; *Sasaki et al*., 2004]. Based on the Modular Ocean Model (MOM3), OFES has a near-global domain extending from 75°S to 75°N but excluding the Arctic Ocean. It has a horizontal resolution of 0.1°and 54 vertical levels.

A climatological solution (CLIM run) is obtained by integrating OFES from a state of rest with annual-mean temperature and salinity from the World Ocean Atlas 1998 [*Boyer and Levitus*, 1997] for 50 years with monthly climatological forcing from the National Centers for Environmental Prediction/National Center for Atmospheric Research (NCEP/NCAR) reanalysis [*Kalnay et al*., 1996]. Daily output over 1990–1997 of this CLIM run is analyzed in this study. Another hindcast run (QSCAT) is also obtained, forced by daily-mean surface wind from QuikSCAT measurements [*Sasaki and Nonaka*, 2006; *Masumoto*, 2010]. We found that the higher-resolution QuikSCAT winds reproduced variability in the BoB better [*Cheng et al*., 2013], and so we analyzed the QSCAT run for the period 2000–2009.

2.2. Models

2.2.1. $1^1/_2$ Layer Model

To investigate the role of wind forcing on SSH variability, we obtain solutions to a nonlinear, $1^1/_2$ layer reduced-gravity model, which is able to simulate the first-baroclinic-mode response of the upper layer ocean quantitatively [*Qiu and Chen*, 2012]. Its governing equations are

Table 1. The Suite of 1½ Layer Reduced-Gravity Model Experiments

Expt.	Linear/Nonlinear	Forcing Wind
Exp 1	Linear	ERA-I daily wind
Exp 2	Nonlinear	ERA-I daily wind
Exp 3	Linear	Higher frequency
Exp 4	Linear	Lower frequency
Exp 5	Nonlinear	Higher frequency
Exp 6	Nonlinear	Lower frequency

$$\boldsymbol{u}_t+\zeta\boldsymbol{k}\times\boldsymbol{u}=-\nabla E+A_h\nabla^2\boldsymbol{u}+\frac{\boldsymbol{\tau}}{\rho_o h}, \tag{1a}$$

$$h_t+\nabla\cdot(h\boldsymbol{u})=0, \tag{1b}$$

where $\boldsymbol{u}=(u,v)$ is the horizontal velocity vector, $\boldsymbol{\tau}=(\tau^x,\ \tau^y)$ is the wind-stress vector, h is the upper-layer thickness, ρ_o is a reference density, and $A_h=100$ m^2/s is the coefficient of horizontal eddy viscosity. Variable $\zeta=f+\boldsymbol{k}\cdot\nabla\times\boldsymbol{u}$ is the absolute vorticity, $E=g'h+(u^2+v^2)/2$ is the total energy, and $g\prime=0.06$ m/s^2 is the reduced-gravity constant. In the 1½ layer reduced-gravity model, the sea level is given by SSH $=(g'/g)h$, where $g=9.8$ m/s^2 is the gravitational constant. To isolate the impact of the nonlinear terms, we also obtain solutions to a linear version of the equations (1a),

$$\boldsymbol{u}_t+f\boldsymbol{k}\times\boldsymbol{u}=-g'\nabla h+A_h\nabla^2\boldsymbol{u}+\frac{\boldsymbol{\tau}}{\rho_o h}, \tag{2a}$$

$$h_t+H_0\nabla\cdot\boldsymbol{u}=0, \tag{2b}$$

where the background layer thickness is $H_0=150$ m, a value consistent with observed thermocline depths in the EEIO (100–150 m) [*Schott et al*., 2009].

Unless specified otherwise, the model domain has a realistic representation of the boundaries of the Indian Ocean within the region 40°S−40°N and 30°E−110°E. The eastern boundary is closed, so there is no Indonesian Throughflow. Solutions are found numerically on a grid with 0.25° resolution. Forcing is by daily surface wind stress derived from ERA-Interim (ERA-I) surface wind-speed data from the European Centre for Medium-Range Weather Forecasts (ECWMF) product which is available on a 0.75° × 0.75° grid for the period 1979–2015 [*Dee et al*., 2011; http://www.ecmwf.int/products/data/archive/]. Solutions are spun up from an initial state of rest with $h=150$ m throughout the basin. While the model solutions are obtained for the entire wind record of 1979–2015, the analyses reported below are confined to the satellite altimeter period 1993–2012 for consistent comparisons.

To isolate the processes responsible for the SSH variability in the southern BoB, a hierarchy of experiments is performed with modified wind forcings, and with and without nonlinearity. The configurations of each experiment are summarized in Table 1 and will be described in the relevant sections.

2.2.2. LCS Model

Previous studies have indicated that the second baroclinic mode is also important in the equatorial IO [*Han* 2005, 2011]. To explore the impact of higher-order modes on 90–180 day variability, we also obtain solutions to an LCS model. LCS models have been applied in many studies of IO circulation and sea level [e.g., *McCreary*, 1980; *McCreary et al*., 1996; *Miyama et al*., 2003, 2006; *Han* 2005, 2011; *Suresh et al*., 2013]. Our version is a modification of the one discussed in *Miyama et al*. [2006].

The LCS equations are essentially the primitive equations of motion linearized about a background state of rest with Brunt-Väisälä frequency, $N_b(z)$, which is taken to be the annual-mean density field calculated from the World Ocean Database 2001 averaged between 1°S and 1°N and from 40°E to 100°E [*Miyama et al*., 2006]. Vertical eddy viscosity and diffusivity coefficients have the depth-dependent form $\nu(z)=A/N_b^2(z)$ where $A=8.84\times10^{-4}$ cm^2/s^3. Wind-stress enters the ocean as a body force with a vertical structure, $Z(z)$, that is uniform in the upper 10 m and decreases to zero linearly from 10 to 20 m. The ocean bottom is assumed flat with the depth $D=4500$ m.

With these assumptions, solutions can be written as the expansions of the vertical (baroclinic and barotropic) modes of the system,

$$q(x,y,z,t)=\sum_{n=1}^{N}q_n(x,y,t)\psi_n(z), \tag{3}$$

where q is either u, v, or p, and $\psi_n(z)$ is the vertical structure of the n-th mode normalized so that $\psi_n(0)=1$. The expansion coefficients, q_n, satisfy

$$\boldsymbol{u}_{nt}+f\boldsymbol{k}\times\boldsymbol{u}_n=-\frac{1}{\rho_o}\nabla p_n-\frac{A}{c_n^2}\boldsymbol{u}_n+A_h\nabla^2\boldsymbol{u}_n+\frac{Z_n}{H_n}\boldsymbol{\tau}, \tag{4a}$$

$$\frac{1}{c_n^2}p_{nt}+\nabla\cdot u_n=-\frac{A}{c_n^2}p_n, \tag{4b}$$

where c_n is the Kelvin-wave speed of the n-th mode, and $Z_n=\int_{-D}^{0}Z(z)\psi_n(z)dz$ and $H_n=\int_{-D}^{0}\psi_n^2(z)dz$ determine how the wind stress couples to the n-th mode. The sea-level response of each mode is given by $d_n=p_n/g$.

For the first three baroclinic modes, the characteristic speeds are $c_1=$ 282 cm/s, $c_2=$ 175 cm/s, and $c_3=$ 110 cm/s, respectively. The first three values of Z_n are close to unity, and $H_1=$ 278 m, $H_2=$ 181 m, and $H_3=$ 801 m [*Miyama et al*., 2006]. With these values, the second baroclinic mode couples more efficiently to the wind than the first one does ($Z_2/H_2 > Z_1/H_1$). *McCreary et al*. [1993] noted the dominance of the second baroclinic mode in their solution.

As for the $1\frac{1}{2}$ layer models, the domain is a realistic version of the Indian Ocean confined to 30°S−25°N and 35°E−115°E. Solutions to (4) are obtained numerically on a grid with a 0.25° resolution. Wind forcing is by ERA-I winds, and analyses are confined to the period 1993–2012.

3. Spatial and Frequency Structure

3.1. Observations

Figure 1 shows the standard deviation of observed SSH variability band passed at 20–190 days. There are five distinct regions of enhanced variability. In the EEIO and southern BoB, large SSH variability is found along the west coast of Sumatra (Region A), in a zonal band across the Bay centered near 5°N (Region B), and to the east of Sri Lanka (Region C). Farther to the north, it is large in the central BoB (Region D) and along the northwestern boundary (Region E). SSH variance is weak in the vicinity of Andaman and Nicobar Islands. The pattern shown in Figure 1 is similar to that of intraseasonal variability reported by *Cheng et al*. [2013].

Figure 2 plots SSH spectra in each of the five regions. They all have "significant" peaks that extend above the 95% confidence level (dashed curves) and their strength increases with period. In Regions A and B, SSH has significant peaks at 30–60, 90, and particularly 180 days. In Region C, peaks are significant at 30–60 days and 120 days; however, the 90 day peak is markedly weak in comparison to Regions A and B. This outcome is likely due to energy transfer into the intraseasonal band (see section 4.4). Similar to Regions A and B, the 180 day peak is also prominent in Region D but not in Regions C and E. The 180 day variability in the BoB arises almost entirely from the propagation of equatorial signals into the basin [*Han et al*., 2011].

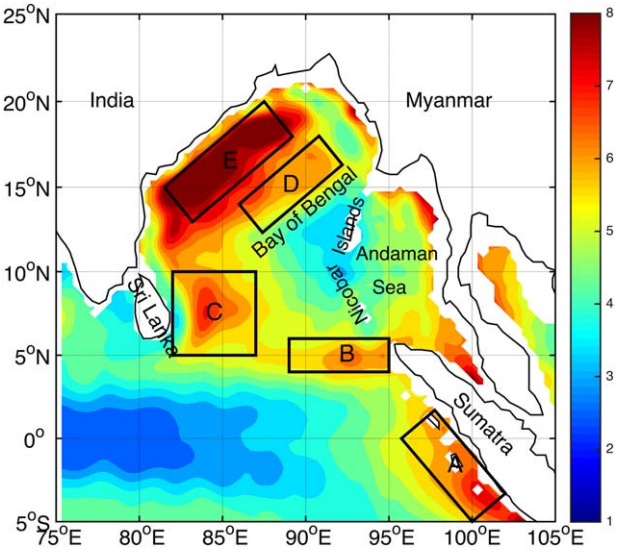

Figure 1. Map of sea-surface-height standard deviation (cm) in the 20–190 day band from satellite observations for the period 1993 − 2012. Boxes indicate the analysis regions considered in the text.

Figure 3 shows the spatial distribution of SSH standard deviation in different period bands. At 30–60 days (Figures 3a), the SSH variance is high across the southern BoB near 5°N, east of Sri Lanka, along the west coast of Sumatra, and along the east coast of the BoB. At these periods, the critical latitudes for the first-baroclinic-mode Rossby waves (poleward of which they do not exist) are located near 5°N−10°N. Therefore, the strong variance along the east coast north of 10°N is mainly caused by coastally trapped, Kelvin (shelf) waves, with no energy being radiated into the interior of the BoB via Rossby waves. At 90–120 days (Figures 3b and 3c), the SSH variability is high in the northwestern BoB. At 180 days (Figure 3d), it is high in the EEIO, especially along the southwestern coast of Sumatra.

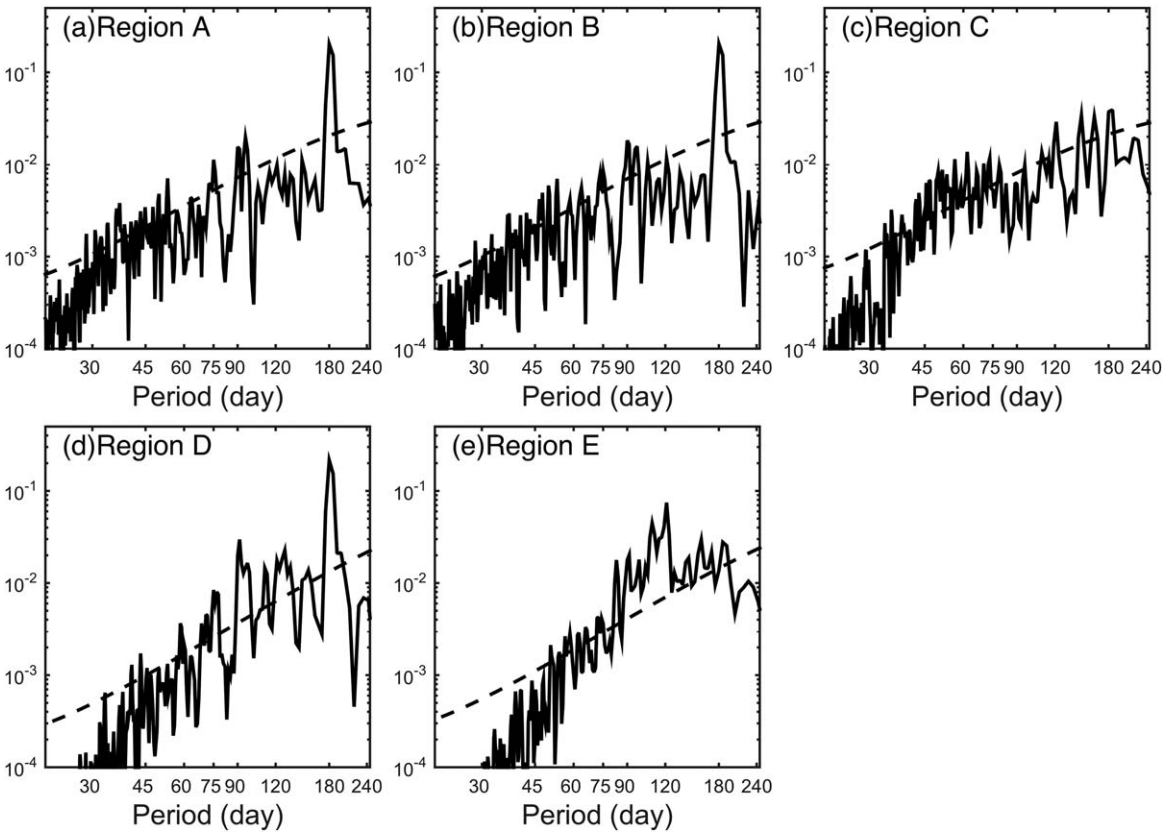

Figure 2. Power spectra for observed sea-surface height with the climatological monthly mean removed. Regions A−E are given by the boxes in Figure 1. The dashed curves indicate 95% confidence levels.

3.2. OFES Solutions

Figure 4 shows SSH standard deviation maps in different period bands from QSCAT and CLIM, respectively. The QSCAT run reproduces the SSH variability in each period band quite well (compare Figures 3 and 4). In contrast, although SSH variability in CLIM remains high in the western BoB, it is weak in the EEIO, around the perimeter of the BoB and east of Sri Lanka (compare plots 4a−4d and plots 4e−4h). A comparison between QSCAT and CLIM highlights the importance of forcing by high-frequency winds in Regions A, B, C, and around the perimeter of the BoB. Interestingly, at 180 days the spatial distribution of SSH standard deviation in CLIM is significantly weaker than in QSCAT (compare Figures 4d and 4h), a consequence of weaker wind forcing at 180 days in CLIM.

Intraseasonal SSH signals propagate eastward along the equator as equatorial Kelvin waves, and reflects from the eastern boundary as coastal Kelvin waves and, provided that their period is longer than 30 days, into a packet of Rossby waves as well [*Cheng et al*., 2013]. As a result, the SSH signals is intensified through the "piling up" or removal of water from along the western coast of Sumatra (Region A). The Rossby-wave packet extends to the "critical latitude" above which Rossby waves no longer exist [*Moore*, 1968; *McCreary*, 1980; *Clarke and Shi*, 1991]. The critical latitude for 30–60 day Rossby waves is located from 5°N to 10°N, which likely is the reason for the high variance in Region B (Figures 3a and 4a).

4. Generation Mechanism of 30–60 Day SSH Variability

4.1. Mechanism Implied by OFES QSCAT

Eddy energy is a good indicator of the intraseasonal SSH variability. Using the QSCAT run, eddy kinetic energy (EKE) and eddy potential energy (EPE) per unit mass are calculated by

$$EKE = \frac{1}{2}\left(u'^2 + v'^2\right), \tag{5}$$

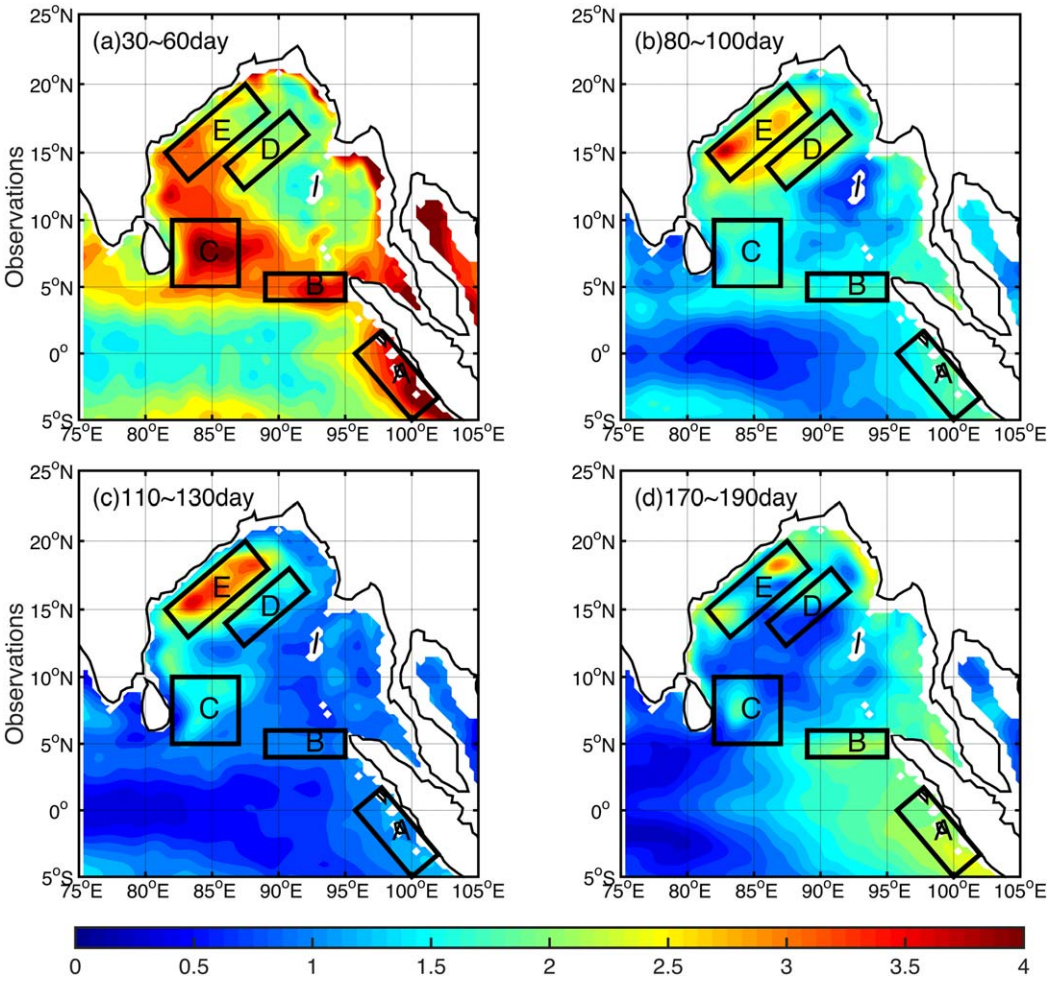

Figure 3. Maps of sea-surface height standard deviation (cm) from satellite observations for the period 1993–2012, showing variability in the (a) 30–60 day, (b) 80–100 day, (c) 110–130 day, and (d) 170–190 day period bands.

$$EPE = -\frac{g\tilde{\rho}'^2}{2\rho(\partial\bar{\rho}_\theta/\partial z)}, \tag{6}$$

where $\tilde{\rho}(x,y,z,t)=\rho(x,y,z,t)-\rho_b(z)$, $\rho_b(z)$ is a background density profile given by the annual and horizontal mean within the BoB, and $\bar{\rho}_\theta$ is the annual and horizontal mean potential density. Transient components of velocity and density (primed quantities) are defined as variability at periods of 30–60 days, with longer-period variations considered to be part of the basic state.

Figure 5a shows that the vertically integrated EKE is weak throughout the basin, with relatively larger values in the southern BoB. In contrast, the vertically integrated EPE is strong west of northern Sumatra, east of Sri Lanka, and western BoB between 10°N and 15°N (Figure 5b). The EPE pattern at 30–60 days is quite different from that at 30–120 days, the latter having a maximum in the northwestern BoB mainly caused by baroclinic instability [*Cheng et al.*, 2013, Figure 13b]. At 30–60 days, EPE dominates the total eddy energy (TEE, sum of EKE and EPE). Along 7.5°N, EKE is strong in the upper 70 m and weakens rapidly with depth (Figure 5c). In contrast, EPE is highest in the depth range of the thermocline (70–150 m), where $\tilde{\rho}'$ is largest, with a maximum between 82°E−87°E (Figure 5d).

Figure 6 shows time-longitude plots of 30–60 day SSH and vertically integrated EPE from surface to 200 m depth along 7.5°N during 2000–2004. Alternating positive and negative SSH signals propagate westward from the eastern boundary to just east of Sri Lanka. The SSH signals are enhanced as they propagate westward, reaching a maximum in Region C (Figure 6a). Propagating features of EPE are very similar to those of 30–60 day SSH, suggesting that the propagation of EPE accounts for the 30–60 day SSH propagation in the southern BoB.

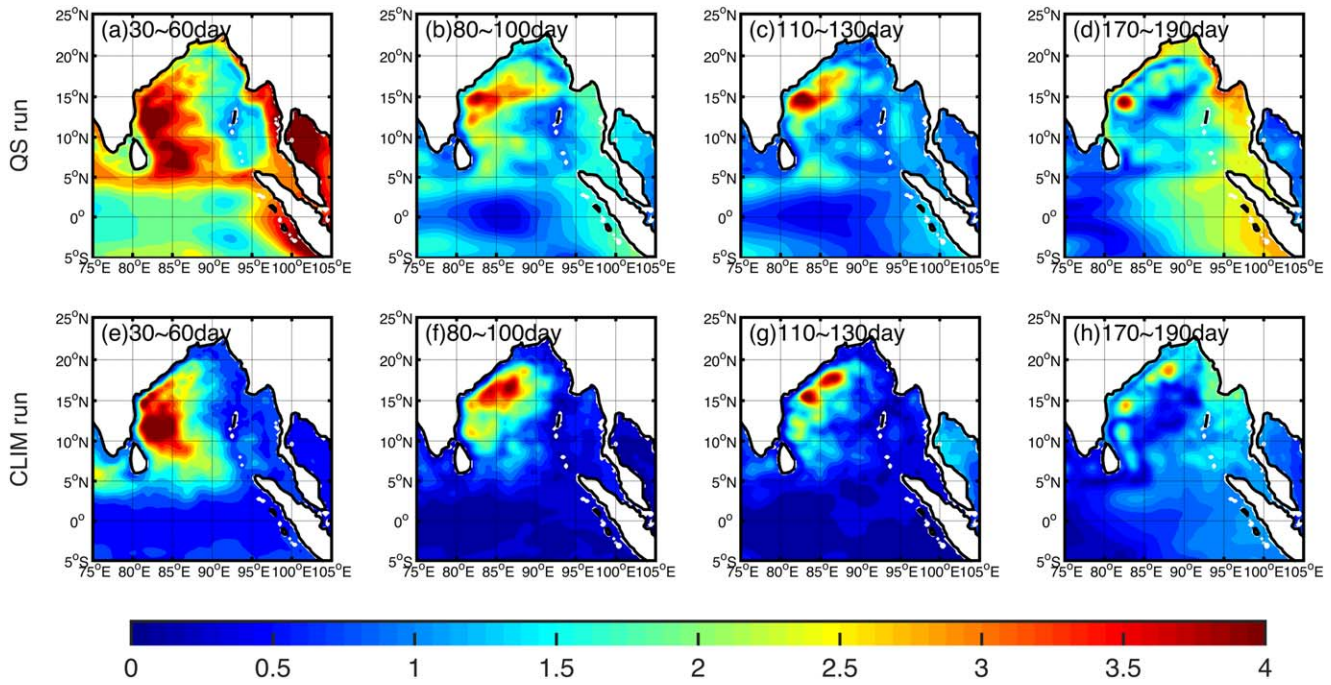

Figure 4. Maps of sea-surface height standard deviation (cm) from the OFES QSCAT run for the period 2000 − 2008, showing variability in the (a) 30 − 60 day, (b) 80 − 100 day, (c) 110 − 130 day, and (d) 170 − 190 day period bands. (e)− h) Same as Figures 4a−4d, but for CLIM run.

The coherent spatial patterns between the vertically integrated EPE and 30–60 day SSH variability (Figure 6) demonstrate that the propagating features along 7.5°N are baroclinic in nature. The high EPE is located in the thermocline layer, demonstrating that EPE and SSH variations at 30–60 days are mainly associated with

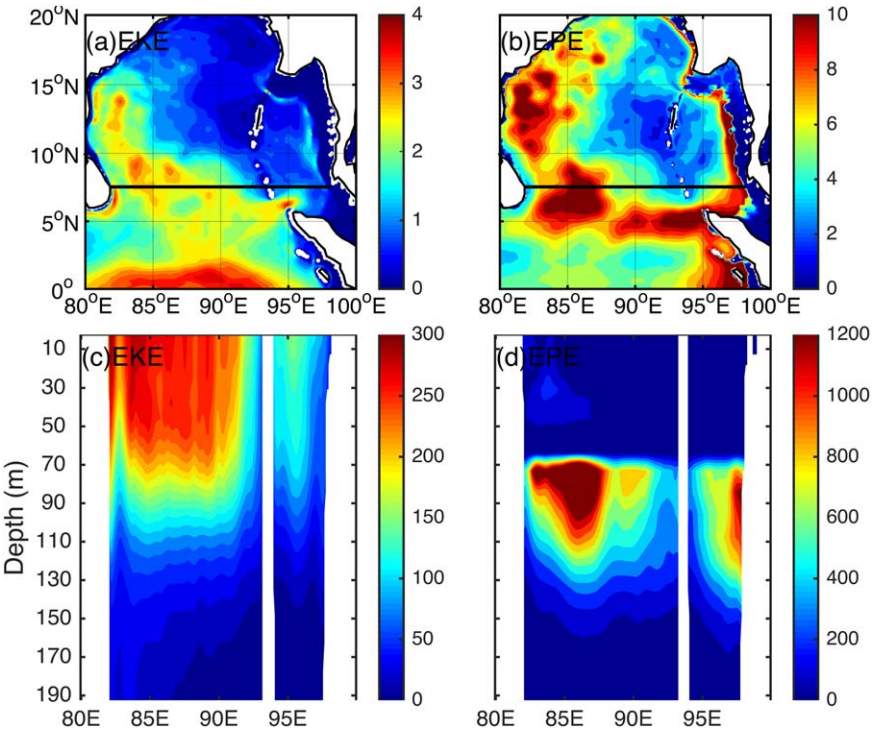

Figure 5. Annual mean vertically integrated (a) eddy kinetic energy (EKE) and (b) eddy potential energy (EPE) (unit: 10^6 cm^3/s^2) in the upper 200 m derived from the QSCAT run. Vertical sections of annual mean (c) EKE and (d) EPE (unit: cm^2/s^2) along 7.5°N indicated by the black lines in Figures 5a and 5b.

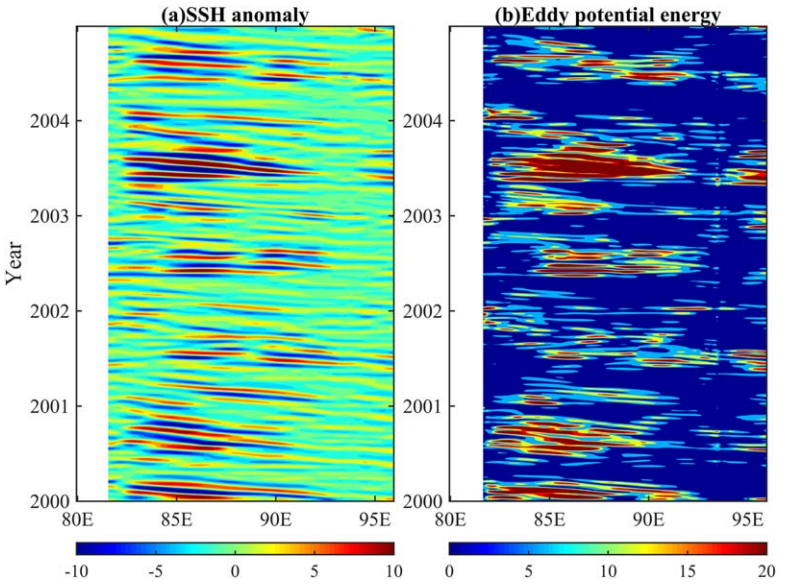

Figure 6. (a) Time longitude plots of 30–60 day sea-surface height anomaly (unit: cm) along 7.5°N from the OFES QSCAT run for the period 2000–2004 (unit: cm). (b) Same as Figure 6a, but for the vertically integrated eddy potential energy in the upper 200 m (unit: 10^6 cm^3/s^2).

the thermocline motions (Figure 5d). The fluctuation of thermocline alters $\tilde{\rho}'$ and further induces the variability of EPE (equation (6)). Since EPE is mostly determined by thermocline motions, we infer that they are associated with the first-baroclinic-mode variability. As such, they can be captured by the $1^1/_2$ layer (reduced-gravity) model.

4.2. Solutions to Linear and Nonlinear $1^1/_2$ Layer Reduced-Gravity Models

Exps 1 and 2, forced by ERA-I winds, reproduce the observed patterns of intraseasonal SSH variance in the southern BoB (compare Figure 3a to Figures 7a and 7b). Similar to the observations and QSCAT run, both solutions have high variance in Regions A and B and along the east coast of the BoB. Furthermore, the nonlinear response is qualitatively better (more enhanced) than the linear one along 5°N−10°N, pointing toward the importance of nonlinear interactions there (see sections 4.4 and 4.5). In Region C, the SSH amplitude due to local Ekman pumping is only 20% of observed SSH variability (figure not shown), demonstrating that the local wind forcing accounts for only a small part of the SSH variability at 30–60 days.

4.3. Eddy Forcing in Region C

Figure 8 illustrates the time evolution of both observed and modeled 30–60 day SSH in the southern BoB. In the observations (Figures 8a–8d), on 3 October, there is an anticyclonic (red) eddy in the box east of Sri

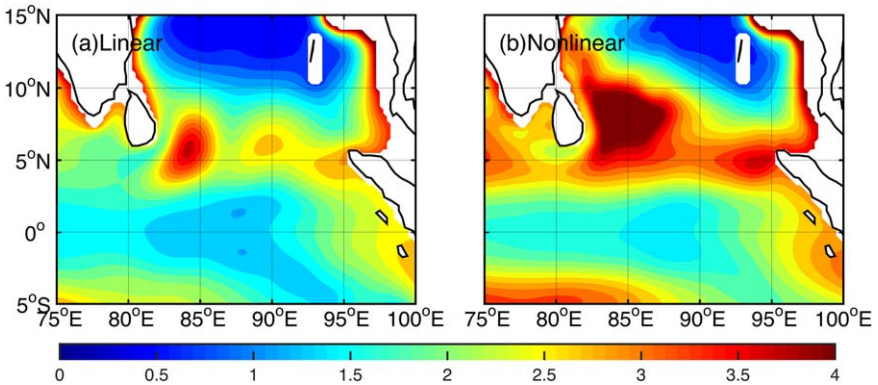

Figure 7. (a) Standard deviation of (a) 30–60 day sea-surface height (cm) from the period 1993–2012 for the solution to the linear, $1^1/_2$ layer model (Exp 1) forced by ERA-I daily wind. (b) Same as Figure 7a, except for the nonlinear model (Exp 2).

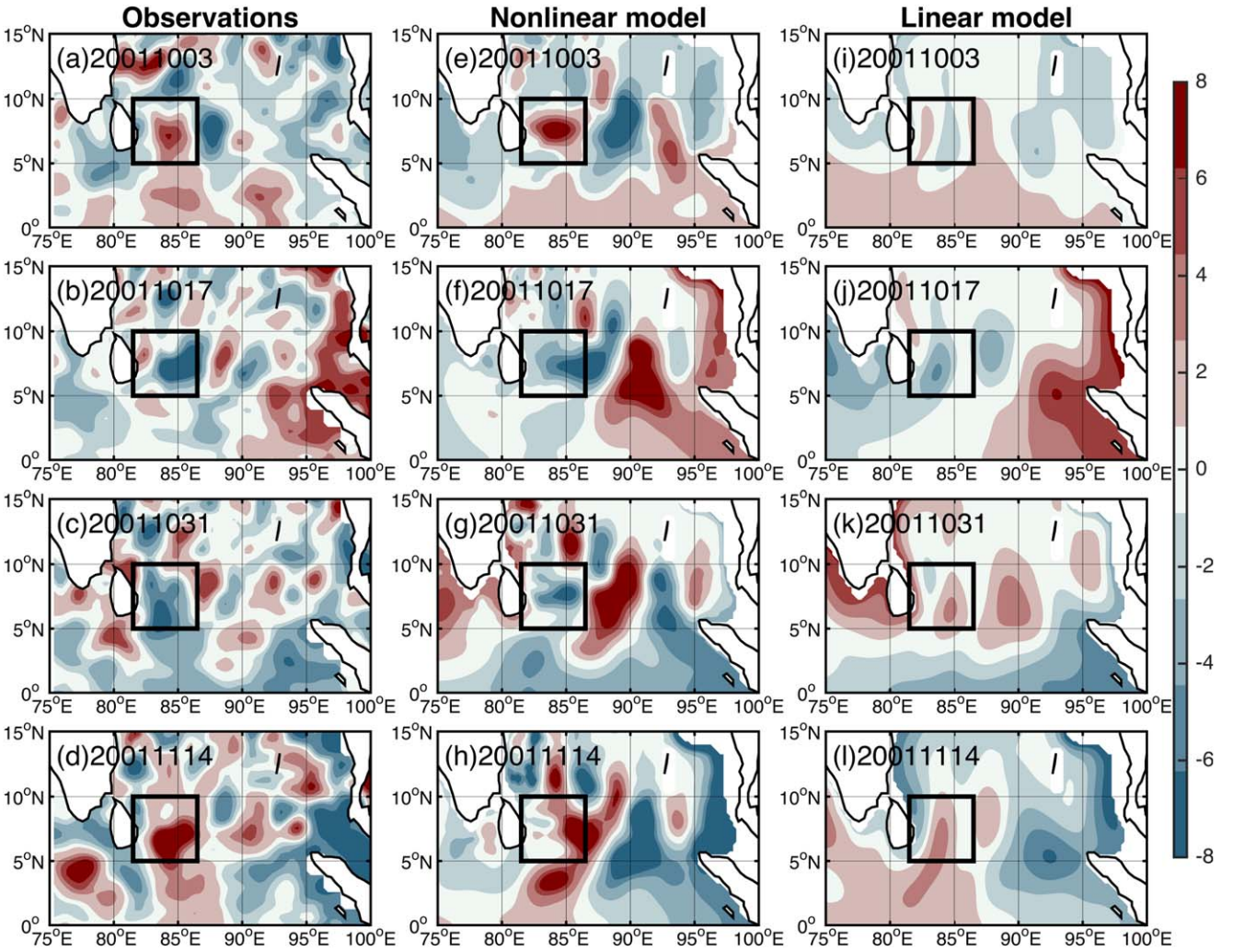

Figure 8. Biweekly snapshots of 30–60 day sea-surface height from 3 October 2001 to 14 November 2001 for (left) satellite observations, and (middle) the solutions to the nonlinear and (right) linear $1\frac{1}{2}$ layer model.

Lanka (Region C) and a cyclonic (blue) eddy east of it. From 10 to 31 October, the anticyclonic eddy dissipates and the cyclonic eddy propagates into the box. On 14 November, the cyclonic eddy dissipates and a second anticyclonic eddy propagates into Region C from the east. These westward-propagating eddies (nonlinear Rossby waves) account for the high variance east of Sri Lanka.

Figures 8a–8d also show the reflection of equatorial Kelvin waves from the eastern boundary, a downwelling event (red) from 3 to 17 October and an upwelling event (blue) from 24 October to 14 November. Subsequently, the coastal signals propagate westward, with strongest amplitude along 5°N−10°N. For example, the red eddy east of Region C on 14 November arose from the coastal downwelling on 17 October. Similarly, the blue eddy east of Region C on 12 December originated from eastern-boundary upwelling on 7 November (figure not shown). Thus, there is a close connection between the nonlinear eddies that enter Region C and the equatorial wind forcing.

Figures 8e–8h plot 30–60 day SSH anomalies from Exp 2, the solution to the nonlinear model forced by ERA-I winds. East of 90°E, there is a similarity to the observed anomalies in Figures 8a–8d. The alternate upwelling and downwelling equatorial Kelvin waves are reproduced. Similar eddies occur near and within Region C, with an anticyclonic (cyclonic) eddy located in Region C on 3 October and 14 November (17–31 October). The eddies are not generated randomly, but rather are linked to the Rossby waves that reflect from the eastern boundary (see next paragraph and section 4.5). Both the nonlinear and linear model can reproduce the Rossby waves radiated from the eastern boundary quite well. Because nonlinearity is strong

in this region, the phase of simulated eddies east of Sri Lanka is not always exactly consistent with observations.

Figures 8i–8l show 30–60 day SSH anomalies from Exp 1, the solution to the linear model forced by ERA-I winds. In this solution, the reflection of the upwelling and downwelling, equatorial Kelvin waves, and the offshore propagation of reflected Rossby waves along 5°N are more evident, because the amplitudes of smaller-scale features are weaker. A careful comparison of the snapshots in Figures 8e–8h and 8i−8l, however, shows that many smaller-scale features occur in both solutions, albeit with different amplitudes, indicating that much of the response in Figures 8i–8l is wind-driven. On the other hand, variability near Region C differs significantly between Exps 1 and 2, pointing toward the importance of nonlinear interactions there.

4.4. Nonlinear Transfers in Region C

To determine why the 30–60 day SSH variance is stronger in Region C in the nonlinear model than in the linear model, we obtained Exps 3–6, which use ERA-I winds that are high-passed (<70 days) and low-passed (>70 days) to force the linear and nonlinear models, respectively. Figure 9 shows the resulting SSH standard deviation at 30–60 days for the two nonlinear solutions: Exp 5, forced by high-passed winds (Figure 9a), and Exp 6 forced by low-passed winds (Figure 9b).

Surprisingly, the nonlinear response to high-passed forcing (Figure 9a) is essentially unchanged from that of the linear solution (Exp 3, not shown). This similarity is surprising, given the significant differences between the linear and nonlinear solutions at intraseasonal time scales (Figure 7): It implies that the differences must be caused by nonlinear transfer from lower frequencies into the intraseasonal band. The intraseasonal response to low-passed winds in the linear solution is zero (not shown). In contrast, the nonlinear response has significant variability in intraseasonal bands (Figure 9b), again indicating that nonlinear transfer must be taking place.

Figure 10 shows the power spectra of simulated SSH in Region C for Exps 3–6. When forced by high-passed winds, intraseasonal SSH peaks show little or no difference at 30–60 days between the linear (Exp 3; plot a) and nonlinear (Exp 5: plot c) solutions. When forced by low-passed winds, the 90–120 day peaks present in the linear solution (Exp 4; plot b) are much weaker in the nonlinear one (Exp 6; plot d), whereas peaks at 30–60 days are enhanced in the nonlinear solution. These properties confirm the nonlinear transfer as suggested by the standard-deviation maps.

4.5. Dynamics of Wave-to-Eddy Transition

To explore the dynamics of energy transfer and eddy formation, we carried out several idealized experiments. *Suresh et al*. [2013] suggested that 80–90% of intraseasonal SSH variance in the eastern BoB is due to equatorial remote forcing. To explore this idea, we forced the $1\frac{1}{2}$ layer model with a patch of equatorial, zonal wind stress τ^x. It is confined to the region 50°E−90°E, 5°S−5°N, oscillates at a period of 90 days; its amplitude is a maximum of 0.1 dyn cm^{-2} in the center of the region, and

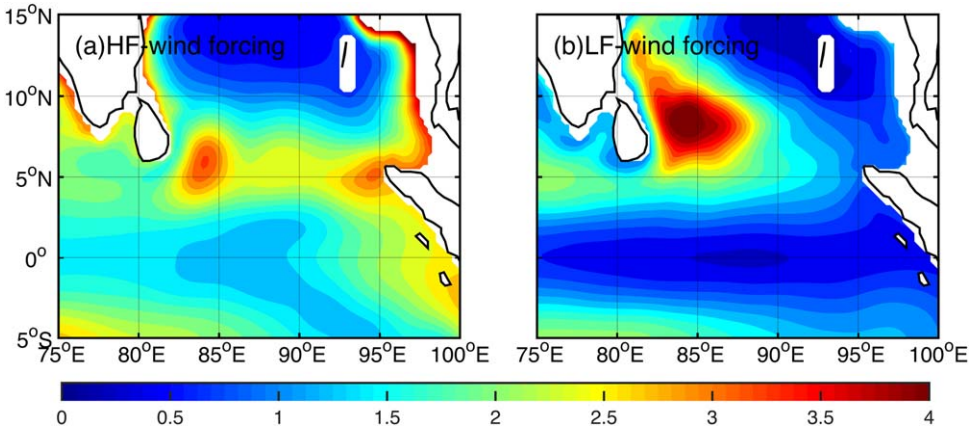

Figure 9. Maps of 30–60 day sea-surface height standard deviation (cm) from the nonlinear, $1\frac{1}{2}$ layer model forced by (a) high-passed (<70 days) and (b) low-passed (>70 days) ERA-I daily winds for the period 1993–2012.

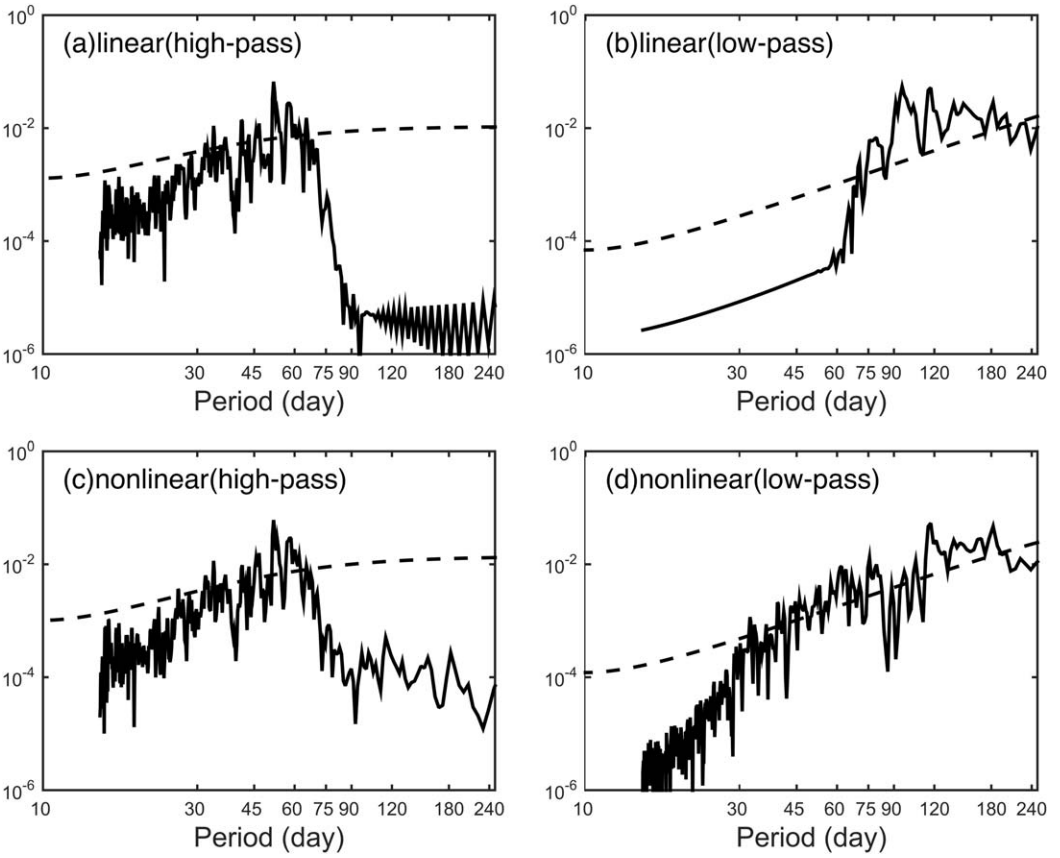

Figure 10. Sea-surface height power spectra in Region C from four 1½ layer solutions: (a) linear model forced by high-passed (<70 days) ERA-I winds, (b) linear model forced by low-passed (>70 days) winds, (c) same as Figure 10a except for nonlinear model, and (d) same as Figure 10b except for nonlinear model. The 95% confidence level is shown by the dashed curve.

decreases sinusoidally to zero at its edges. The model basin is a rectangle within the region 40°S−40°N and 30°E−100°E.

In a linear version of the model (Figures 11a–11d), a sequence of linear baroclinic Rossby waves radiate from the eastern boundary, with phase lines that tilt southwest-northeast due to their faster speed at lower latitudes. No isolated eddies are formed. In the nonlinear version, however, when Rossby waves propagate westward from the eastern boundary, they become unstable and begin to form isolated mesoscale eddies (Figure 11e–11h). At 30–60 days, cold and warm eddies seem to be generated near 90°E abruptly and are enhanced rapidly when they propagate westward (Figure 11i–11l).

Figure 12 shows power spectra of SSH anomalies averaged within the box in Figure 11. In the linear model, the ocean has only a 90 day response to the 90 day wind forcing, while the 90 day variance are much weaker in the interior basin for the nonlinear model. Variability at 90 days transfers energy to the 20–45 day band as it propagates westward.

Figure 13 illustrates the SSH anomalies for the solutions to the nonlinear layer model with a real coastline, forced by the same equatorial zonal wind stress. Basic properties of the SSH anomalies are similar to those in Figures 11g and 11k, indicating that the coastline does not significantly alter the phase and amplitude of the waves and eddies.

The above idealized experiments offer an explanation for the generation and propagation of eddies in the southern BoB: Lower-frequency Rossby waves, generated by the reflection of equatorial signals [*Cheng et al*., 2013; *Girishkumar et al*., 2013; *Suresh et al*., 2013], radiate from the eastern boundary, and they become nonlinearly unstable near 90°E to generate eddies; the instability transfers energy to higher-frequency variability, which enhances the 30–60 day variability east of Sri Lanka (Figures 11 and 12). So like Regions A and

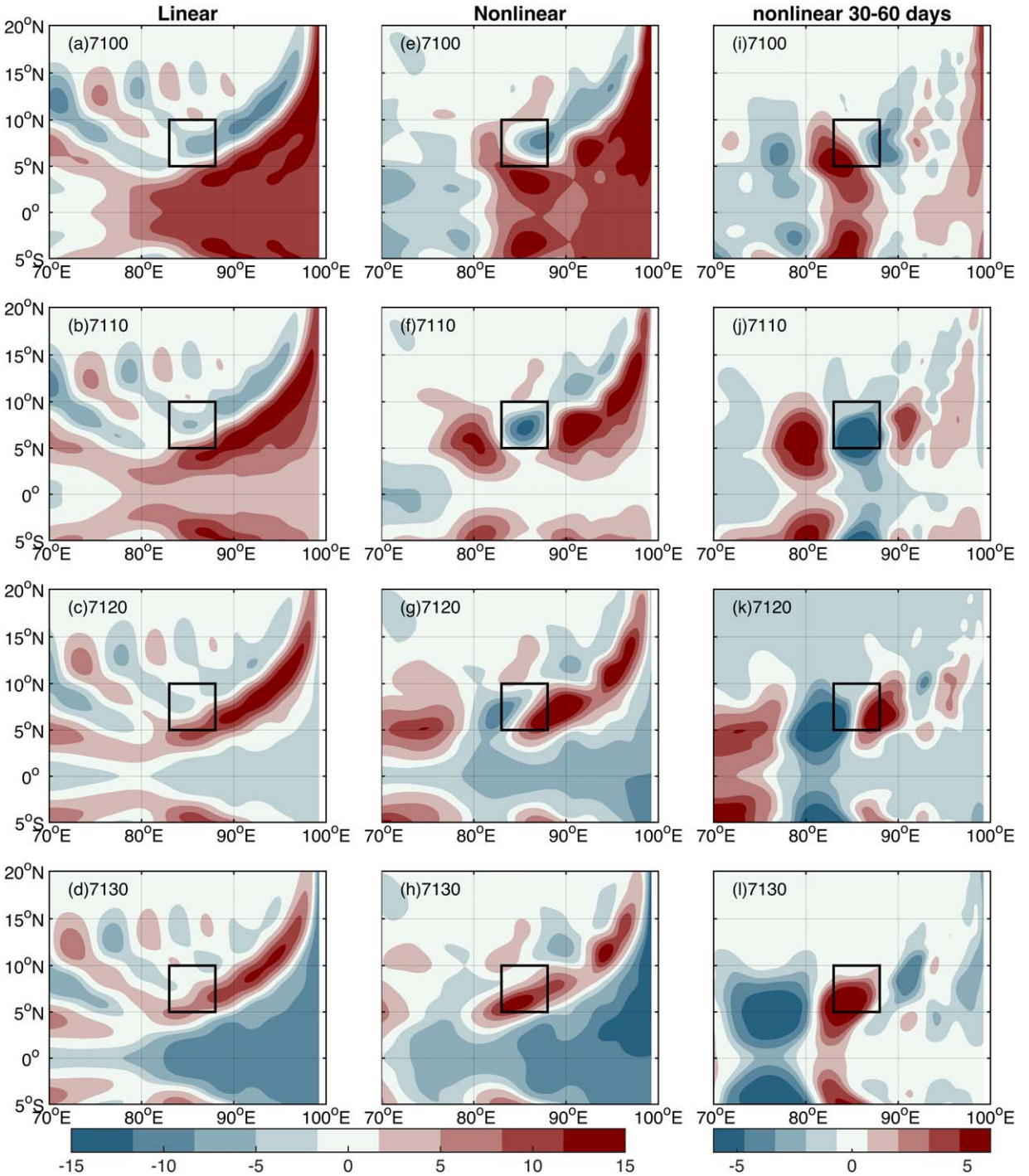

Figure 11. Ten days snapshots of sea-surface height anomalies from 7100 day to 7130 day for the solutions to (left) linear and (right) nonlinear $1\frac{1}{2}$ layer model. The model basin is a box within the region 40°S−40°N and 30°E−100°E, forced by a patch of zonal wind stress τ_x oscillating at a period of 90 days. The wind patch is confined to the region 50°E−90°E, 5°S−5°N, its peak amplitude is 0.1 dyn cm^{-2}, and it decreases sinusoidally to zero at the edges of the region. Right plots same as middle plots but for 30–60 day signals.

B, SSH variability east of Sri Lanka (Region C) is also largely driven by equatorial processes. We note that this physical situation is similar to the one studied by *Qiu et al.* [2013], except that his forcing period was the annual cycle. His solution also developed eddies due to nonlinearity, specifically to triad interactions among reflected Rossby waves. It is not clear if the same process accounts for eddy generation in our situation.

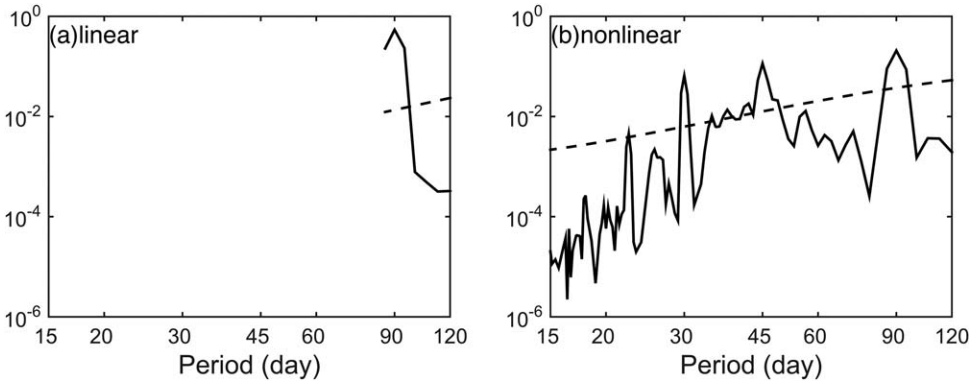

Figure 12. Power spectra of sea-surface height averaged within the box in Figure 11 from (a) linear and (b) nonlinear $1^1/_2$ layer model. The 95% confidence level is shown by the dashed curve.

5. Generation Mechanism of 90–180 Day SSH Variability

5.1. Importance of the $n=2$ Mode

Previous studies suggested that resonances in the equatorial IO occur for the $n=2$ mode near 90 and 180 days, and therefore enhance the signals in both of those period bands [*Jensen*, 1993; *Han* 2005; *Han et al*., 2011]. The $n=2$ mode is absent in the $1^1/_2$ layer model, so we obtain solutions to the LCS model to investigate the 90–180 day SSH variability. *Han et al*. [2011] studied the basin resonances using idealized winds with uniform amplitude at all periods. In our analysis, we also force solutions with realistic wind amplitudes, in order to understand better their impact in the real ocean.

Figure 14 plots the SSH standard deviations from the LCS solution forced by ERA-I winds, showing contributions for the $n=1$ and $n=2$ responses, as well as their sum ($n=1+2$), in the 90, 120, and 180 day bands. In the 90 and 120 day bands, the SSH variance for the $n=2$ mode is a little weaker than that for the $n=1$ mode, and the $n=1+2$ responses are close to the observations in the southern BoB. At 180 days, the SSH variance is dominated by the $n=2$ mode, with a similar pattern and comparable amplitude to those observed; the amplitude of the $n=1+2$ response is somewhat stronger than observed (Figures 14i and 4f).

The LCS solutions indicate that at 180 days the $n=2$ baroclinic mode contributes significantly along the west coast of Sumatra, in the southern BoB and around the perimeter of the basin. The contributions from higher-order modes ($n > 2$) are very small, and essentially have no significant impact on the 180 day response.

5.2. Resonance

Following *Han et al*. [2011], the condition for basin resonance is

$$T=4L/(mc_n), \tag{7}$$

where T is the wind forcing period, L is the width of Indian Ocean at the equator ($\approx$ 6491 km), and $m=1, 2, \cdots$ is a positive integer. For the $n=1$ mode, $c_1=$ 282 cm/s and (7) gives $T \approx$ 107 days when $m=1$. For

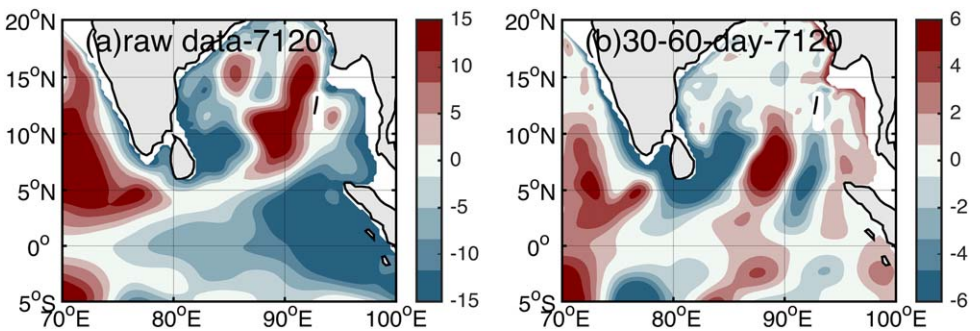

Figure 13. (a) Snapshot of sea-surface height anomalies (cm) on 7120 day from the nonlinear, $1^1/_2$ layer model with real coastline forced by a patch of zonal wind stress τ_x, which is same as the wind used in Figure 11. (b) Same as Figure 13a but for 30–60 day signals.

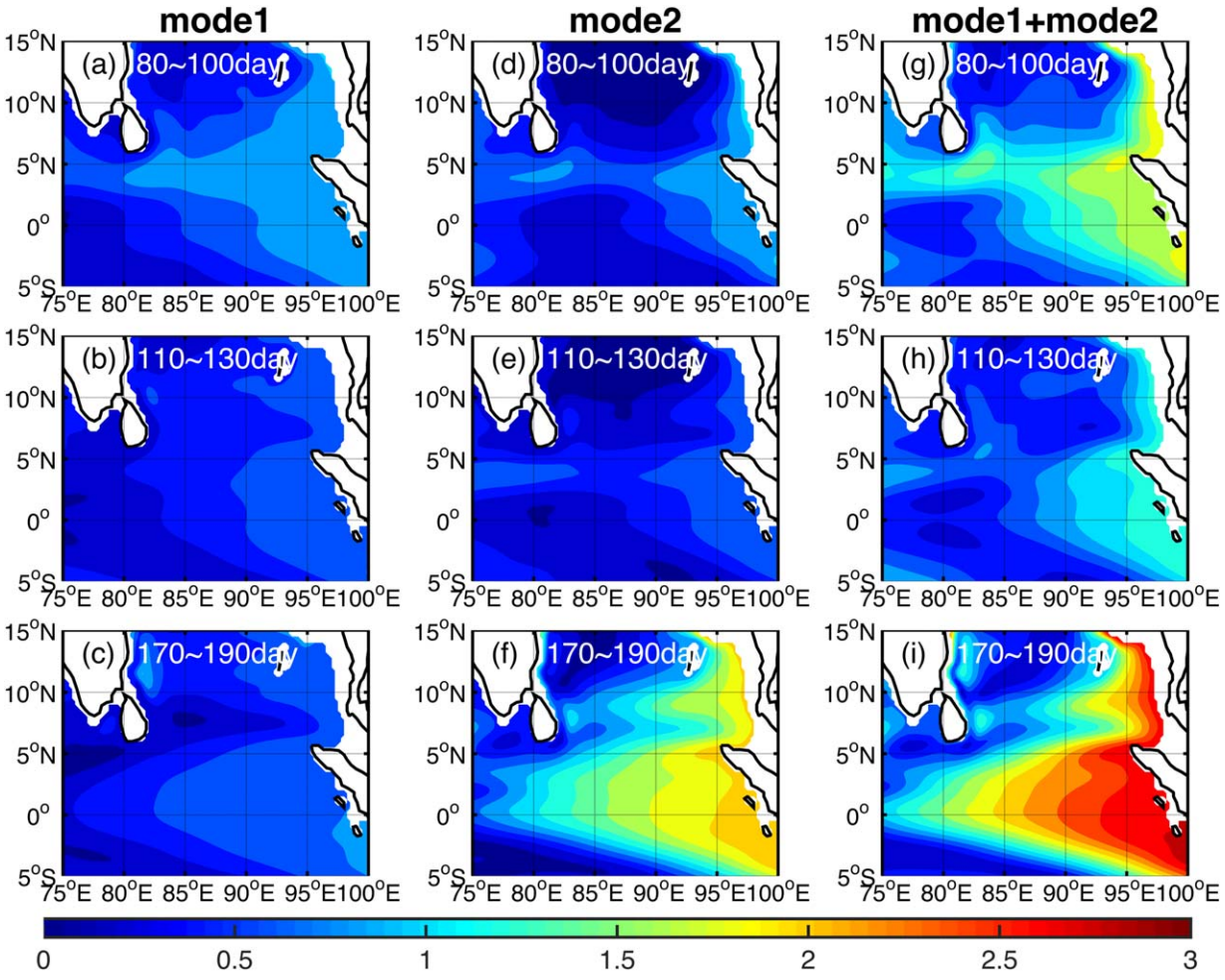

Figure 14. Maps of sea-surface height standard deviation (cm) from the LCS solution forced by ERA-I winds for the period 1993–2012, showing variability for the (left) $n=1$ mode, (middle) $n=2$ mode, and (right) their sum in the (top) 90 day, (middle row) 120 day, and (bottom) 180 day period bands.

the $n=2$ mode, $c_2 = 175$ cm/s and the resonant periods are $T \approx 172$ days for $m=1$ and $T \approx 86$ days for $m=2$. Resonance periods in the LCS model are slightly shorter than those in *Han et al.* [2011], due to the faster phase speeds c_n.

Figure 15a shows SSH in the eastern equatorial IO driven by a patch of zonal wind stress τ_x with an amplitude of 0.15 dyn cm^{-2} and for a range of periods. For the $n=1$ mode, the curve shows a peak near 120 days and a trough near 180 days, whereas for the $n=2$ mode the maximum occurs near 175 days with a secondary peak at 80–100 days. The resonant peaks are broad, so even though the resonant peaks occur at 85, 107, and 170 day periods in our solutions, we can see resonant strengthening of the 90, 120, and 180 day responses, as discussed in *Han et al.* [2011]. In general, SSH variance at 140–250 days for the $n=2$ mode is stronger than that for the $n=1$ mode, an indication that the second baroclinic mode couples more efficiently to the wind.

In the real ocean, the spatial structure and amplitude of winds vary with period. Figure 15b shows the SSH amplitudes forced by the ERA-I winds at different periods from the LCS model. The SSH peaks appear sharper than those forced by ideal winds, a consequence of the variation in wind amplitude. In the equatorial IO, the ERA-I winds have their largest amplitude near 180 days, which drives very strong SSH variance at this resonant period for the $n=2$ mode. Even though the $n=1$ mode is not resonant at 180 days (there is a trough in Figure 15a), the 180 day response still shows a peak, again due to the strong 180 day forcing by the ERA-I winds. At 90–120 days, the amplitude of SSH variance for the $n=1$ mode is comparable to that for the $n=2$ mode. Due to the weaker resonance and wind strength, SSH variance at 80–120 days is weaker than that at 180 days.

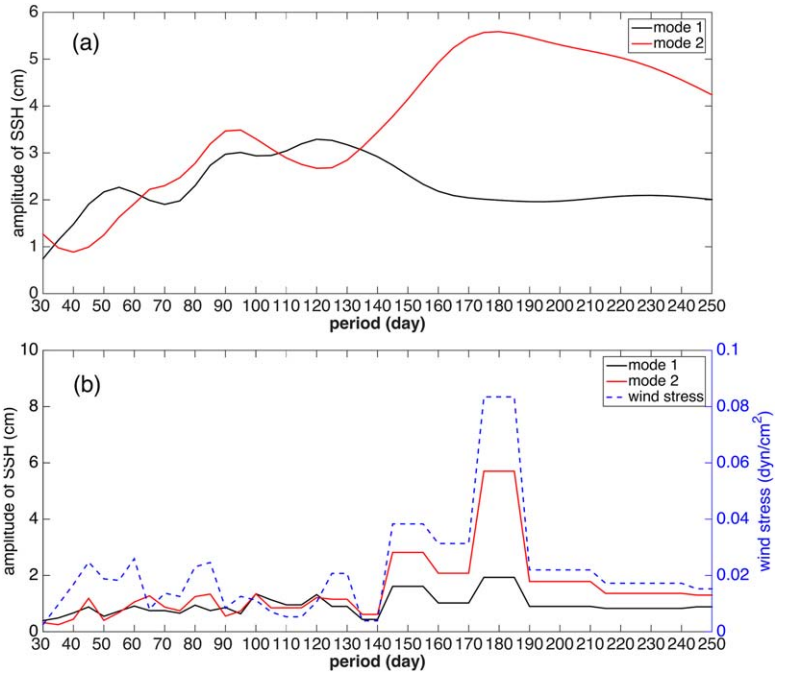

Figure 15. (a) SSH amplitudes for the first two vertical modes of the LCS model, averaged over the region, 75°E−105°E, 5°S−5°N. The curves are obtained from a series of solutions forced by a patch of zonal wind stress τ_x oscillating at a range of periods (T=30, 35, ⋯ 250 days). The wind patch is confined to the region 30°E−100°E, 15°S−15°N, its peak amplitude is 0.15 dyn cm^{-2}, and it decreases sinusoidally to zero at the edges of the region. Results shown are from year 5, when solutions are close to equilibrium. (b) Same as Figure 15a, but for LCS solutions forced by ERA-I winds for the period 1993 − 2012, superimposed on the amplitude of equatorial zonal wind stress (5°S−5°N average).

6. Summary

In this study, we discuss SSH variability in the BoB and EEIO at periods from 30–180 days, and explore the mechanisms that cause the variability in the southern BoB using 1½ layer and LCS models. There are five regions where the SSH variability attains relative maxima (Figure 1). We investigate the mechanisms that cause the variability in the southern BoB (Regions A, B, and C). Intraseasonal SSH variability in Regions A and B appears to be largely driven by the equatorial processes: Equatorial signals first radiate into the BoB and around its perimeter via coastal Kelvin waves, and then propagate off the eastern boundary as Rossby waves [e.g., *Vialard et al*., 2009; *Cheng et al*., 2013; *Suresh et al*., 2013].

At 30–60 days, high SSH variance is found in a zonal band across the Bay centered near 5°N, along the west coast of Sumatra and around the perimeter of BoB and east of Sri Lanka. The nonlinear 1½ layer reduced-gravity model reproduces the SSH variability in the southern BoB quite well, especially to the east of Sri Lanka. Local forcing has little contribution to the SSH variability east of Sri Lanka, while eddies (nonlinear Rossby waves) propagating from the east play a primary role. In the nonlinear 1½ layer model, variability at 90–120 days transfers energy to that at 30–60 days, indicating the importance of nonlinear processes. In support of this conclusion, we obtained idealized solutions forced by a patch of equatorial zonal wind oscillating at 90 days: In this solution, 90 day Rossby waves generated by the reflection of equatorial signals, become nonlinearly unstable near 5°N−10°N, 90°E, generating eddies with a higher-frequency variability.

Previous studies, based on linear theory, attribute 30–60 day variability in the equatorial Indian Ocean to MJO wind forcing only [e.g., *Han et al*., 2001; *Han* 2005; *Oliver and Thompson*, 2010]. Our study suggests that it can also obtain energy from lower-frequency variability through nonlinear processes: Just equatorward of the critical latitude for 30–60 day variability, longer-period, reflected Rossby waves become nonlinearly unstable, forming mesoscale eddies at some distance away from the eastern boundary. This sequence of events is similar to that found for the annual period by *Qiu et al*. [2013], but we have not demonstrated that the eddy generation at 30–60 days results from the same process (triad interactions).

At 90–120 days, SSH variance is very strong in the northern BoB (Regions D and E), while weak in the southern BoB. In comparison to Regions A and B, the 90 day peak east of Sri Lanka is markedly weak (Figure 2), likely due to the energy transfer into the shorter intraseasonal band (Figure 10). At 180 days, high variance appears in eastern BoB (Regions A and B). Solutions to the LCS model suggest that in the southern BoB the $n=2$ mode is dominant at 180 days, due to basin resonance and strong wind forcing.

In conclusion, we have shown that the SSH variability in southern BoB (Figure 1) results from the equatorial processes. Further, linear dynamics accounts for its basic features, with the exception that some energy is transferred nonlinearly into the 30–60 day band. In the northern BoB, the SSH is not as clearly linked to the equatorial processes. Further, baroclinic instability, which is absent in our $1\frac{1}{2}$ layer and LCS models, is dynamically important [*Cheng et al.*, 2013]. We plan to extend our present study to investigate the SSH variability in the northern Bay in a future study.

Acknowledgments

The OFES output used in this study is obtained from APDRC, University of Hawaii (http://apdrc.soest.hawaii.edu). The AVISO product is obtained from CNES (http://www.aviso.altimetry.fr). We thank Toru Miyama at JAMSTEC for providing us the code of the linear, continuously stratified model. This study benefited from discussions with Zuojun Yu. This research was supported by the Natural Science Foundation of China (41522601, 41525019, and 41521005), the "Strategic Priority Research Program" of the Chinese Academy of Sciences (XDA11010103), the State Oceanic Administration of China (GASI-IPOVAI-02), and the Open Project Program of State Key Laboratory of Tropical Oceanography (grant LTOZZ1501). X.H.C. is also sponsored by the Pear River S&T Nova Program of Guangzhou (201506010036). Much of this research was carried out while Xuhua Cheng visited Julian McCreary at the International Pacific Research Center at the University of Hawaii.

References

Boyer, T. P., and S. Levitus (1997), *Objective Analyses of Temperature and Salinity for the World Ocean on a 1/4° Grid, NOAA/NESDIS Atlas*, vol. 11, 62 pp., U.S. Gov. Policy Off., Washington, D. C.

Chen, G., W. Han, Y. Li, D. Wang, and T. Shinoda (2015), Intraseasonal variability of upwelling in the equatorial Eastern Indian Ocean, *J. Geophys. Res. Oceans*, *120*, 7598–7615, doi:10.1002/2015JC011223.

Cheng, X., S.-P. Xie, J. P. McCreary, Y. Qi, and Y. Du (2013), Intraseasonal variability of sea surface height in the Bay of Bengal, *J. Geophys. Res. Oceans*, *118*, 816–830, doi:10.1002/jgrc.20075.

Clarke, A. J., and C. Shi (1991), Critical frequencies at ocean boundaries, *J. Geophys. Res.*, *96*, 10,731–10,738.

Dee, D. P., et al. (2011), The ERA-Interim reanalysis: Configuration and performance of the data assimilation system, *Q. J. R. Meteorol. Soc.*, *137*, 553−597, doi:10.1002/qj.828.

Dibarboure, G., O. Lauret, F. Mertz, and V. Rosmorduc (2008), *SSALTO/DUACS User Handbook: (M) SLA and (M) ADT Near-Real Time and Delayed Time Products, SALP-MU-P-EA-21065-CLS*, 1.9 ed., 39 pp., Agne, France. [Available at http://www.aviso.oceanobs.com/fileadmin/documents/data/tools/hdbk_duacs.pdf.]

Girishkumar, M. S., M. Ravichandran, M. J. McPhaden, and R. R. Rao (2011), Intraseasonal variability in barrier layer thickness in the south central Bay of Bengal, *J. Geophys. Res.*, *116*, C03009, doi:10.1029/2010JC006657.

Girishkumar, M. S., M. Ravichandran, and W. Han (2013), Observed intraseasonal thermocline variability in the Bay of Bengal, *J. Geophys. Res. Oceans*, *118*, 3336−3349, doi:10.1002/jgrc.20245.

Han, W. (2005), Origins and dynamics of the 90-day and 30–60-day variations in the equatorial Indian Ocean, *J. Phys. Oceanogr.*, *35*, 708−728.

Han, W., J. P. McCreary, D. L. T. Anderson, and A. J. Mariano (1999), Dynamics of the eastward surface jets in the equatorial Indian Ocean, *J. Phys. Oceanogr.*, *29*, 2191−2209.

Han, W., D. M. Lawrence, and P. J. Webster (2001), Dynamical response of equatorial Indian Ocean to intraseasonal winds: Zonal flow, *Geophys. Res. Lett.*, *28*, 4215−4218.

Han, W., J. P. McCreary Jr., Y. Masumoto, J. Vialard, and B. Duncan (2011), Basin resonances in the equatorial Indian Ocean, *J. Phys. Oceanogr.*, *41*, 1252–1270, doi:10.1175/2011JPO4591.1.

Iskandar, I., and M. J. McPhaden (2011), Dynamics of wind forced intraseasonal zonal current variations in the equatorial Indian Ocean, *J. Geophys. Res.*, *116*, C06019, doi:10.1029/2010JC006864.

Jensen, T. G. (1993), Equatorial variability and resonance in a wind-driven Indian Ocean model, *J. Geophys. Res.*, *98*, 22,533–22,552.

Kalnay, E., et al. (1996), The NCEP/NCAR 40-year reanalysis project, *Bull. Am. Meteorol. Soc.*, *77*, 437−471, doi:10.1175/1520-0477077<0437:TNYRP>2.0.CO;2.

Masumoto Y. (2010), Sharing the results of a high-resolution ocean general circulation model under a multi-discipline framework?: A review of OFES activities, *Ocean Dyn.*, *60*(3), 633−652, doi:10.1007/s10236-010-0297-z.

Masumoto, Y., et al. (2004), A fifty-year eddy-resolving simulation of the world ocean: Preliminary outcomes of OFES (OGCM for the Earth Simulator), *J. Earth Simul.*, *1*, 35−56.

McCreary, J. P. (1980), Modeling wind-driven ocean circulation, *Tech. Rep. HIG-80-3*, 64 pp., Hawaii Inst. Geophys., Honolulu.

McCreary, J. P., P. K. Kundu, and R. L. Molinari (1993), A numerical investigation of dynamics, thermodynamics and mixed-layer processes in the Indian Ocean, *Prog. Oceanogr.*, *31*, 181−244.

McCreary, J. P., W. Han, D. Shankar, and S. R. Shetye (1996), On the dynamics of the East India Coastal Current 2: Numerical solutions, *J. Geophys. Res.*, *101*, 13,993−14,010.

Miyama, T., J. McCreary, T. Jensen, J. Loschnigg, S. Godfrey, and A. Ishida (2003), Structure and dynamics of the Indian-Ocean cross-equatorial cell, *Deep-Sea Res., Part II*, *50*, 2023−2047.

Miyama, T., J. P. McCreary Jr., T. G. Jensen, D. Sengupta, and R. Senan (2006), Dynamics of biweekly oscillations in the equatorial Indian Ocean, *J. Phys. Oceanogr.*, *36*, 827–846, doi:10.1175/JPO2897.1.

Moore, D. W. (1968), Planetary-gravity waves in an equatorial ocean, Ph.D. thesis, 201pp., Harvard Univ., Cambridge, Mass.

Moore, D. W., J. P. McCreary Jr., T. G. Jensen, D. Sengupta, and R. Senan (2006), Dynamics of biweekly oscillations in the equatorial Indian Ocean, *J. Phys. Oceanogr.*, *36*, 827−846, doi:10.1175/JPO2897.1.

Oliver, E. C. J., and K. R. Thompson (2010), Madden-Julian Oscillation and sea level: Local and remote forcing, *J. Geophys. Res.*, *115*, C01003, doi:10.1029/2009JC005337.

Qiu, B., and S. Chen (2012), Multidecadal sea level and gyre circulation variability in the northwestern tropical Pacific Ocean, *J. Phys. Oceanogr.*, *42*, 193−206, doi:10.1175/JPO-D-11-061.1.

Qiu, B., S. Chen, and H. Sasaki (2013), Generation of the North Equatorial Undercurrent Jets by triad baroclinic Rossby wave interactions, *J. Phys. Oceanogr.*, *43*(12), 2683–2698, doi:10.1175/JPO-D-13-099.1.

Rio, M. H., S. Guinehut, and G. Larnicol (2011), New CNES-CLS09 global mean dynamic topography computed from the combination of GRACE data, altimetry, and in situ measurements, *J. Geophys. Res.*, *116*, C07018, doi:10.1029/2010JC006505.

Sasaki, H., and M. Nonaka (2006), Far-reaching Hawaiian Lee countercurrent driven by wind-stress curl induced by warm SST band along the current, *Geophys. Res. Lett.*, *33*, L13602, doi:10.1029/2006GL026540.

Sasaki, H., et al. (2004), A series of eddy-resolving ocean simulations in the world ocean: OFES (OGCM for the Earth Simulator) project, in *Proceedings of the Oceans'04/MTS/IEEE/Techno- Ocean'04*, vol. 3, pp. 1535−1541, Cobe, Japan.

Schott, F. A., S.-P. Xie, and J. P. McCreary Jr. (2009), Indian Ocean circulation and climate variability, *Rev. Geophys.*, *47*, RG1002, doi:10.1029/2007RG000245.

Suresh, I., J. Vialard, M. Lengaigne, W. Han, J. McCreary, F. Durand, and P. M. Muraleedharan (2013), Origins of wind-driven intraseasonal sea level variations in the North Indian Ocean coastal waveguide, *Geophys. Res. Lett.*, *40*, 5740−5744, doi:10.1002/2013GL058312.

Vialard, J., S. S. C. Shenoi, J. P. McCreary, D. Shankar, F. Durand, V. Fernando, and S. R. Shetye (2009), Intraseasonal response of the northern Indian Ocean coastal waveguide to the Madden-Julian Oscillation, *Geophys. Res. Lett.*, *36*, L14606, doi:10.1029/2009GL038450.

Vinayachandran, P. N., C. P. Neema, S. Mathew, and R. Remya (2012), Mechanisms of summer intraseasonal sea surface temperature oscillations in the Bay of Bengal, *J. Geophys. Res.*, *117*, C01005, doi:10.1029/2011JC007433.

Volkov, D. L., G. Larnicol, and J. Dorandeu (2007), Improving the quality of satellite altimetry data over continental shelves, *J. Geophys. Res.*, *112*, C06020, doi:10.1029/2006JC003765.

Webber, B. G. M., A. J. Matthews, and K. J. Heywood (2010), A dynamical ocean feedback mechanism for the Madden-Julian Oscillation, *Q. J. Meteorol. Soc.*, *136*, 740−754, doi:10.1002/qj.604.